Computation of Supersonic Flows over Three-Dimensional Configurations

Kuo-Yen Szema,* William L. Riba,* Vijaya Shankar,† and Joseph J. Gorski‡
Rockwell International Science Center, Thousand Oaks, California

An aerodynamic prediction technique based on the steady form of the full-potential equation has been applied to a variety of three-dimensional supersonic flow problems exhibiting embedded subsonic regions. A conservative switching scheme is employed to transition from the supersonic marching procedure to a subsonic relaxation algorithm, and vice versa. Numerical solutions are obtained for a number of complex configurations, including advanced tactical fighter, Langley canard-wing fighter configuration, isolated shuttle orbiter, and mated shuttle orbiter configuration with external tank. The computed results are in good agreement with available experimental data.

Nomenclature

a	= speed of sound
a_{11}	= transformation metric $\zeta_x^2+\zeta_y^2$
C_D	= drag coefficient
C_L	= lift coefficient
C_M	= pitch-moment coefficient
C_p	= pressure coefficient
i,j,k	= streamwise, radial, and circumferential indices
J	= Jacobian of transformation
M_∞	= freestream Mach number
q^+	= $[\rho^{*\gamma-1}/m_p^2]^{1/2}$, sonic condition
U,V,W	= contravariant velocities
x,y,z	= Cartesian coordinates
α	= angle of attack
γ	= ratio of specific heats
ζ,η,ξ	= transformed coordinates
ρ	= density
ρ^*	= sonic density
ϕ	= velocity potential
$\hat{\ }$	= wing sweep angle

Introduction

THE prediction of inviscid low supersonic Mach number flowfields about complex three-dimensional configurations is of great interest to both researchers and designers. For treatment of such flows, full-potential methods[1-3] based on a space-marching procedure offer the advantage of requiring only moderate computer resources (memory and time) while maintaining sufficient accuracy.

In the full-potential method of Refs. 1 and 2, the equation is transformed to a generalized, nonorthogonal, curvilinear coodinate system and is solved by a highly efficient, implicit, finite difference scheme based on the characteristic theory of signal propagation. A space-marching technique is used when the flow is supersonic in a given marching direction. If the velocity in the marching direction becomes subsonic, the domain of dependence changes and the marching scheme is modified to a relaxation-type method through a conservative switching operator.

Presented as Paper 85-0272 at the AIAA 23rd Aerospace Sciences Meeting, Reno, NV, Jan. 14-17, 1985; received March 14, 1985; revision received Sept. 10, 1985. Copyright © American Institute of Aeronautics and Astronautics, Inc., 1985. All rights reserved.

*Member Technical Staff. Member AIAA.
†Manager, Computational Fluid Dynamics Department. Associate Fellow AIAA.
‡Senior Technical Associate. Member AIAA.

The presence of subsonic pockets in a supersonic flow occurs very frequently near fuselage-canopy junction areas and wing leading-edge regions. In fact, future design of advanced fighter wings ($M_\infty = 1.2$-2.0, wing sweep ~ 48 deg) will purposely incorporate subsonic regions near the leading edge to benefit from the leading-edge suction peak associated with subsonic flows.

In Ref. 1, a numerical mapping technique is used to generate the body-fitted coordinate system at a marching plane. The key advantage of this method is that it has no restrictions on its applicability to complex geometries and intricate shocked flowfields. In contrast to the general coordinate formulation of Ref. 1, the method of Ref. 3 is based on a spherical plane marching technique and its application to general three-dimensional geometries is yet to be demonstrated.

The main purpose of this study is to investigate the usefulness of the methodology of Ref. 1 in treating supersonic flows with large embedded subsonic regions over complex geometries, including realistic fighter configurations, shuttle orbiter, and multibody configurations (orbiter on top of the external tank/solid rocket boosters) at low supersonic Mach numbers ($M_\infty = 1.2$ to 2.0).

Analysis

The physical and computational coordinate systems are shown in Fig. 1. As discussed in Refs. 1 and 2, the entire flowfield is divided into three regions (see Fig. 2): 1) the pure supersonic region, 2) the marching subsonic region (MSR), and 3) the total subsonic region (TSR). The basic governing equations and boundary conditions are essentially the same as in Ref. 2 and, therefore, only a brief discussion of the method is presented here.

Governing Equation

The conservative form of the full-potential equation cast in an arbitrary coordinate system defined by $\zeta=\zeta(x,y,z)$, $\eta=\eta(x,y,z)$, and $\xi=\xi(x,y,z)$ can be written as

$$\left(\rho\frac{U}{J}\right)_\zeta+\left(\rho\frac{V}{J}\right)_\eta+\left(\rho\frac{W}{J}\right)_\xi=0 \tag{1}$$

where the density is given by

$$\rho=\left[1-\frac{(\gamma-1)}{2}M_\infty^2\left\{U\phi_\zeta+V\phi_\eta+W\phi_\xi-1\right\}\right]^{1/(\gamma-1)} \tag{2}$$

and M_∞ is the freestream Mach number, U,V, and W are the contravariant velocity components, and J is the Jacobian of

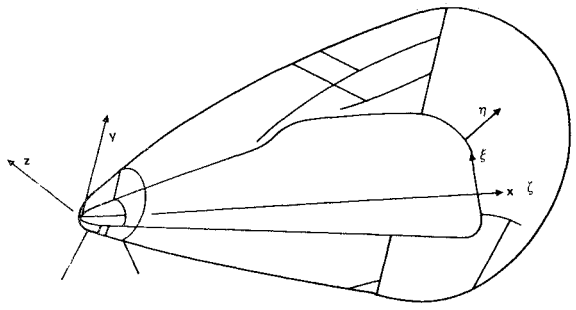

Fig. 1 Computational coordinate system.

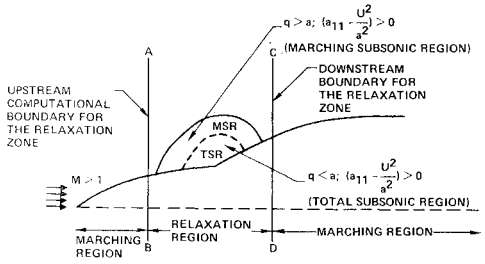

Fig. 2 Embedded subsonic bubble in a supersonic flow.

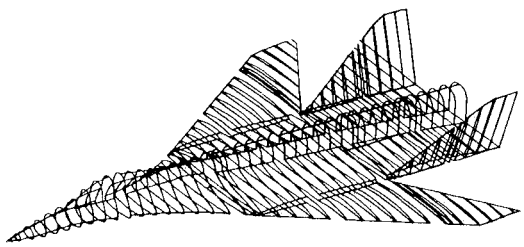

Fig. 3 Fighter-like configuration (ATF).

the transformation. The treatment of each term in Eq. (1), including the density biasing procedure and the implicit approximate factorization algorithm, can be found in Refs. 1 and 2.

Initial Conditions

Supersonic Flow Region

For a pure supersonic flow, initial conditions are required at the starting plane. For sharp-nosed configurations, conical solutions are prescribed, and for a blunt-nosed configuration, the axisymmetric, unsteady, full-potential solver of Ref. 4 is used to obtain the detached bow shock flowfield in the forebody region.

Embedded Subsonic Flow Region

When Eq. (1) is applied at the $(i+1)$ plane within an embedded subsonic region, information on the flux ρU at the $(i+2)$ plane is required. For the first relaxation pass, sonic conditions are assumed at $(i+2)$

$$\rho_{i+2} = \rho^* = \left(\frac{2}{\gamma+1} + \frac{\gamma-1}{\gamma+1} M_\infty^2\right)^{1/\gamma-1} \tag{3}$$

$$U_{i+2} = q^* \sqrt{a_{11_{i+2}}}$$

where

$$q^* = [\rho^{*\gamma-1}/M_\infty^2]^{1/2}$$

Sonic values ρ^* and q^* are purely a function of the freestream Mach number M_∞. The quantity a_{11} is a transformation metric term.

Table 1 Test cases

	Case 1 (Fig. 3)	Case 2 (Fig. 10)	Case 3 (Fig. 12)	Case 4 (Fig. 17)
M_∞	1.6, 1.4	2.0	1.4	1.4
α	See Table 2	4.0	0 deg, −1.94 deg	0 deg

Boundary Conditions

In order to solve the full-potential equation, it is essential to specify appropriate boundary conditions on the body surface and along the outer boundary.

Body Surface

At a solid boundary, the contravariant velocity V is set to zero. Exact implementation of $V=0$ in the implicit treatment of Eq. (2) is described in Ref. 1.

Outer Boundary

The outer boundary is outside the bow shock where the freestream velocity potential ϕ_∞ is imposed. All discontinuities in the flowfield are captured. The precise density biasing activator of Ref. 1, based on the characteristic theory, allows for sharp capturing of shocks in the flow.

Swept Trailing-Edge Wake Treatment

In order to treat the region behind the trailing edge, an artificial cut is created, and the pressure jump $[p]$ across this cut is imposed to be zero as a boundary condition. The full-potential equation is not solved at grid points on the wake cut. Instead, $\phi_{\eta\eta}=0$ is solved to provide $[p]=0$ across the wake cut. A complete discussion of this is given in Ref. 2.

Method of Solution

Figure 2 shows the schematic of a fuselage-canopy forebody geometry with an embedded MSR and TSR present in a supersonic flow. To solve this problem, the marching scheme of Ref. 1 is used when $(a_{11} - U^2/a^2)$ is negative, and a relaxation scheme is used when $(a_{11} - U^2/a^2)$ is positive.

First, march from the nose up to the plane denoted by A-B in Fig. 2, using the method of Ref. 1. Then, between planes A-B and C-D, which embed the subsonic bubble (MSR and TSR), use a relaxation scheme and iterate until the subsonic bubble is fully captured. Finally, resume the marching scheme from the plane C-D downstream of the body.

Geometry and Grid System

The geometry of a configuration is prescribed at discrete points in a cross plane (usually $x=$ constant planes) at various axial locations. These geometry input points are usually obtained from a geometry package such as GEMPAK[5] or CDS.[6] The input points are then divided into several patches, and at each patch a key-point system is established. The geometry at a marching plane is then obtained by joining appropriate key points for each patch. Using a cubic spline passing through the key points, a desired grid-point distribution (clustering) is set up on the body surface. Then, by choosing an appropriate outer boundary, the grid for the flowfield calculation is generated by using an elliptic grid generator. More discussions can be found in Ref. 2.

Results

Results for the following five different configurations are presented to demonstrate the versatility and robustness of the code in handling a wide variety of nonlinear flows:

Case 1: Advanced tactical fighter configuration (Fig. 3).
Case 2: Langley canard-wing fighter configuration (Fig. 8).
Case 3: Isolated shuttle orbiter (Fig. 12).
Case 4: Multibody configuration: shuttle orbiter with external tanks/solid rocket boosters (Fig. 17).

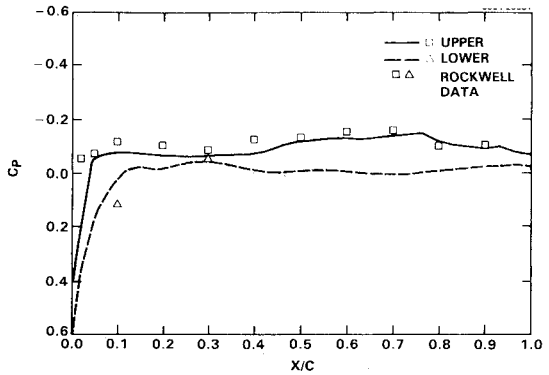

Fig. 4 ATF chordwise pressure distribution; $M_\infty = 1.6$, $\alpha = 1.24$, $Z = 183$ in.

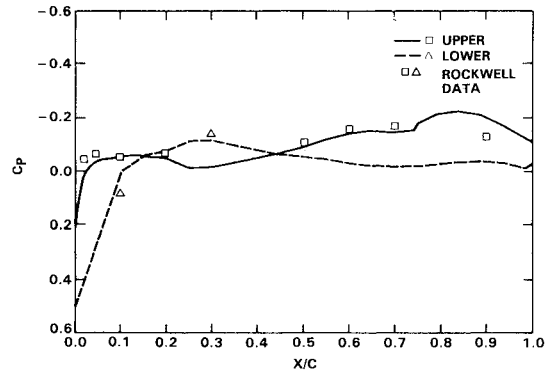

Fig. 5 ATF chordwise pressure distribution; $M_\infty = 1.6$, $\alpha = 1.24$, $Z = 245$ in.

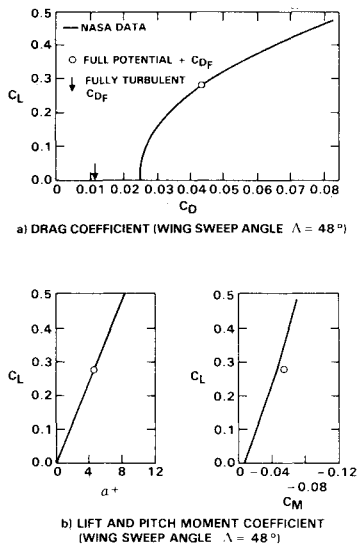

Fig. 6 Comparison of measurement and full-potential prediction at $M = 1.6$ for 48 deg sweep linear multipoint design wing.

Table 2 Test cases for the advanced tactical fighter configuration

	α	5°	4.5°	5°	4.5°
	M_∞	1.6[a]	1.6[b]	1.4[b]	1.6[b]
	Λ	48°	48°	48°	55°
C_L	Code	0.298	0.3016	0.3561	0.29186
	Data	0.277	0.295	0.342	0.283
C_D	Code	0.0482	0.04916	0.04117	0.0404
	Data	0.0457	0.0493	0.0426	0.0396

[a]Without vertical tail. [b]With vertical tail. Λ = wing sweep angle.

The test conditions for each of these cases are summarized in Table 1.

Case 1

Figures 4 and 5 show the chordwise pressure distribution on the upper and lower surfaces at 60% (183 in.) and 80% (245 in.) span stations, respectively. The results show that the present predictions are in very good agreement with Rockwell's experimental data.

Figure 6 shows the comparison of overall forces and moments in terms of C_L, C_D, and C_M. The full-potential results compare very well with NASA data. The drag calculation C_D includes the skin-friction and base drag. The computed viscous drag was for a fully turbulent condition at the test unit Reynolds number of 2×10^6. The 48-deg wing sweep results of Fig. 6 correspond to a supersonic leading-edge condition of 3.3 deg. The lift and drag coefficients from the present calculations for this fighter model, at different Mach numbers, are summarized in Table 2. The results are in excellent agreement with experimental data.

Figure 7 shows the grid and pressure contours for the same fighter geometry with a nacelle mounted on the undersurface of the wing. Only the exterior of the nacelle is modeled as part of the wing-body combination. At an axial marching station immediately preceding the inlet face, initial conditions are generated by interpolation from the flowfield without the nacelle. The shock formed around the nacelle near the inlet face (see Fig. 7) is diffused at downstream stations.

Case 2

Figure 8 shows a fighter model tested at NASA Langley that has a canard and a fuselage-mounted flow-through nacelle. The actual computational geometry and the surface grid employed in this study are shown in Fig. 9. Computations were performed for this configuration at $M_\infty = 2$ and $\alpha = 4$ deg. Figure 10 shows results of cross-flow streamlines, surface pressures, pressure contours, and cross-flow velocity vectors at an axial station where the fuselage, wing, canard wake, and nacelle are all presented. The nodal singularity in pressure contour present at lower wing-body junction regions corresponds to a saddle singularity of cross-flow streamlines, as shown in Fig. 10. Note the pressure match along the canard wake cut. The upper and lower center plane pressure contours at $M_\infty = 2.0$ and $\alpha = 4.0$ deg are shown in Fig. 11. The bow shock, canopy shock, nacelle shock, and expansion wave are all nicely presented in this figure.

Case 3

Figures 12-16 give the geometry, the gridding, and the corresponding flowfield solutions of the isolated shuttle orbiter at $M_\infty = 1.4$, $\alpha = 0$, and -1.94 deg. The chordwise pressures on the upper surface are shown in Fig. 13, and they compare very well with the experimental data. Figure 14 shows the circumferential pressure distribution for the orbiter at $x = 1200$ in. It is noted that the pressure along the vertical tail and the

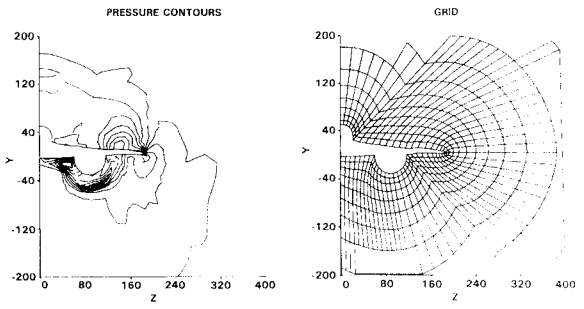

Fig. 7 Pressure contour and grid of ATF with nacelle; $M_\infty = 1.6$, $\alpha = 5$ deg at $x = 375$ in.

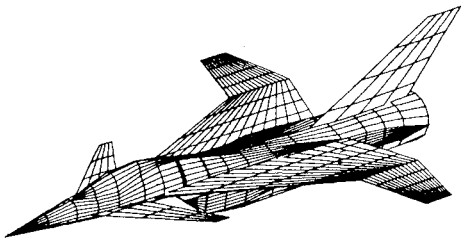

Fig. 8 Langley canard-wing fighter configuration.

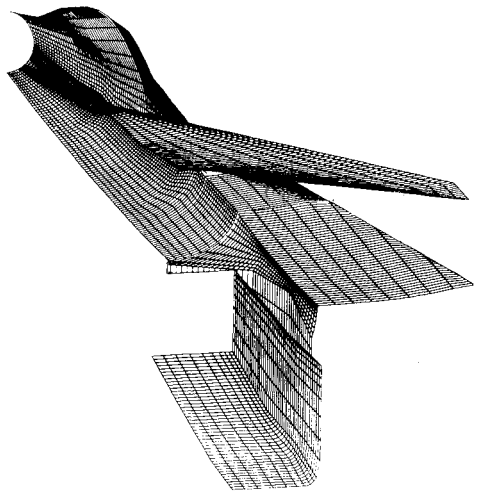

Fig. 9 Computational geometry and surface gridding for Langley fighter configuration.

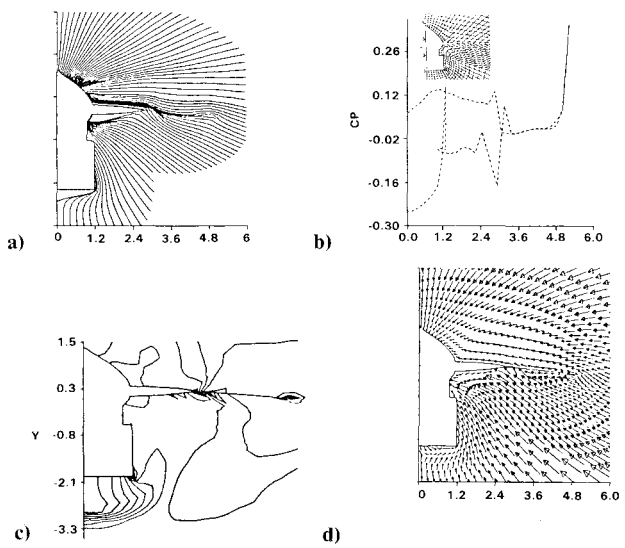

Fig. 10 Solution for Langley figher configuration, $M_\infty = 2.0$, $\alpha = 4.0$, $x = 14.0$; a) Streamline. b) Surface pressure coefficient. c) Pressure contour. d) Velocity vector.

orbital maneuvering subsystem (OMS) pods are well predicted.

Figure 15 shows the details of the orbiter geometry as modeled in this study. The OMS pod is clearly seen in Fig. 15. Figure 16 presents a series of isobar plots at different x locations. The onset of the OMS pod shock formation is clearly seen. The OMS pod shock is formed around $x = 1065$ in., then grows, and finally hits the upper wing surface at approximately $x = 1090$ in. The foot of the OMS pod shock moves further away from the fuselage for increasing x along the orbiter. The trace of the shock foot on the upper surface is also shown

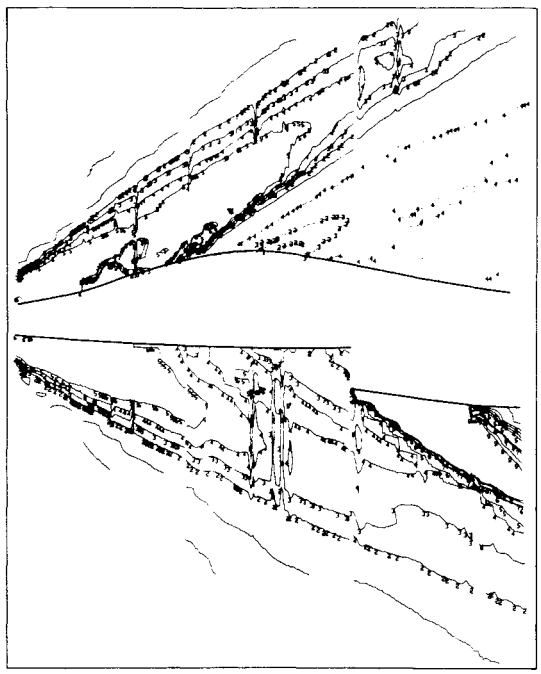

Fig. 11 Upper and lower centerplane pressure contour for Langley fighter configuration; $M_\infty = 2.0$, $\alpha = 4.0$.

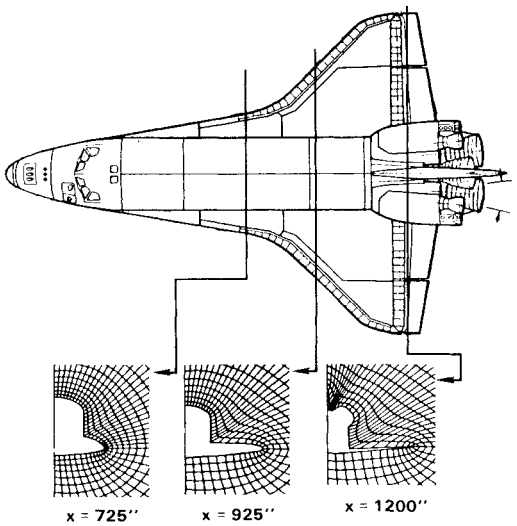

Fig. 12 Shuttle orbiter configuration.

in Fig. 16, and a comparison between the experimental shock and the numerical prediction is made. It should be mentioned that, since the present method is valid for supersonic flow with an embedded subsonic region, it allows one to treat the actual shuttle orbiter without having to make any modifications in geometry.

Case 4

Figure 17 schematically illustrates the multibody interaction problem of the shuttle orbiter in a mated configuration with the external tank (ET) and solid rocket boosters (SRBs) present. Figure 18 shows a perspective view of the complicated multibody problem as modeled by this full-potential code. It is found that the external tank has no effect on the upper wing surface and only a small effect on the lower wing surface of the shuttle orbiter. The high pressure present on the lower surface of the orbiter wing is caused by the aft attach struts that connect the orbiter to the external tank. The presence of the aft attach struts is modeled by a wedge blockage effect and the ET and SRBs are modeled by an elliptic cross-section exter-

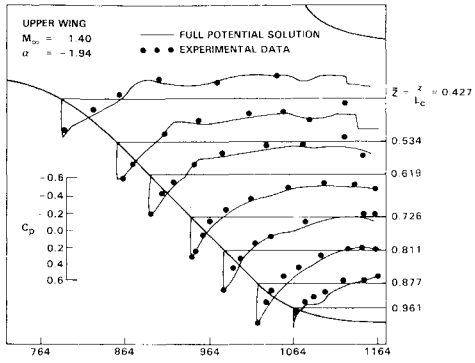

Fig. 13 Shuttle orbiter upper surface pressure distribution.

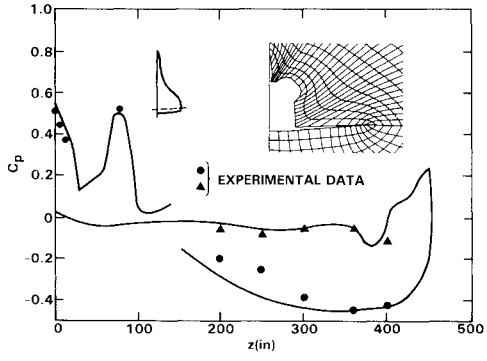

Fig. 14 Circumferential pressure distribution for the orbiter at $x = 1200$ in., $M_\infty = 1.4$, $\alpha = 0$.

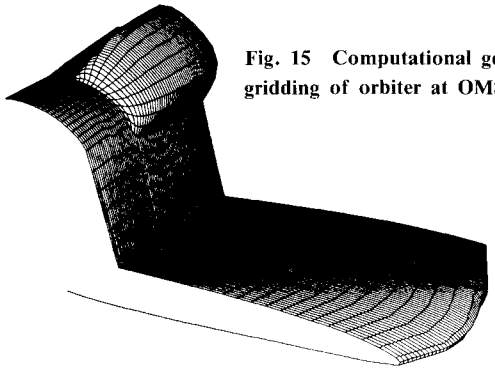

Fig. 15 Computational geometry and gridding of orbiter at OMS pod region.

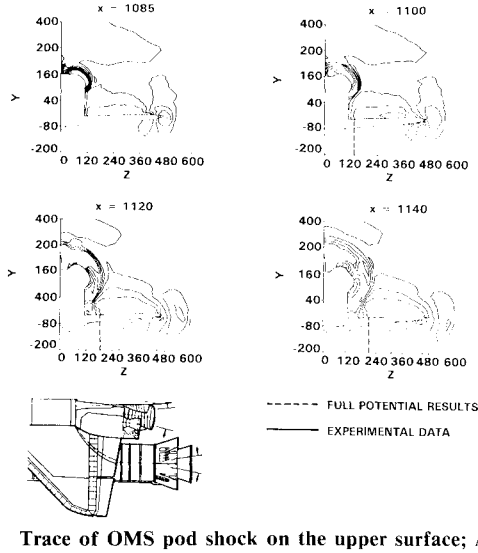

Fig. 16 Trace of OMS pod shock on the upper surface; $M_\infty = 1.4$, $\alpha = 1.94$.

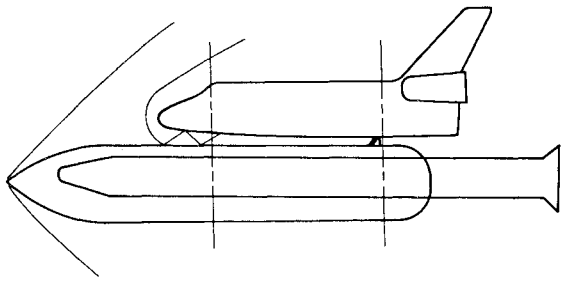

Fig. 17 Orbiter with external tank and SRB.

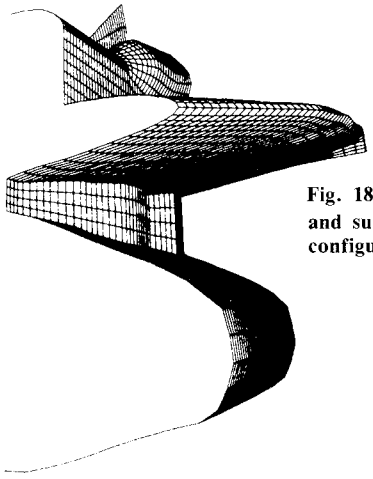

Fig. 18 Computational geometry and surface gridding for mated configuration.

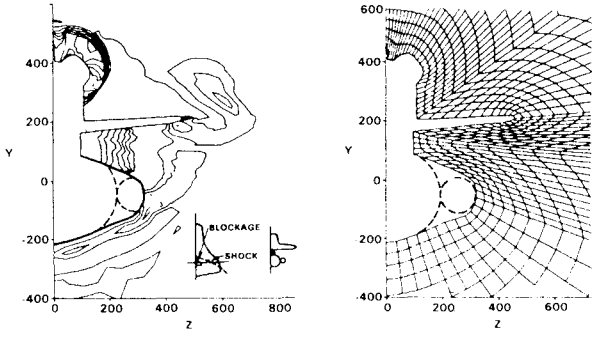

Fig. 19 Gridding and pressure contours for the mated configuration; $M_\infty = 1.4$, $\alpha = 0.0$.

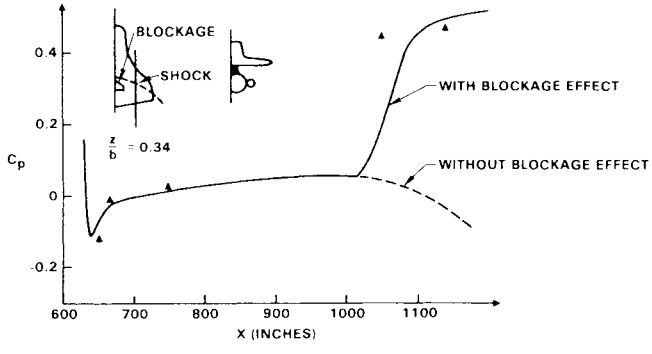

Fig. 20 Orbiter lower surface chordwise pressure distribution; $M_\infty = 1.4$, $\alpha = 0$ deg.

nal tank. Figure 19 shows the gridding and the isobar plot for this multibody problem at an axial station where the wedge blockage effect is present. The detached bow shock formed by the blockage is clearly shown in this figure. Chordwise pressure distribution of the orbiter lower surface at $\bar{z}=0.34$, with and without the blockage, is given in Fig. 20. The result with the blockage effect included shows a very good comparison with the experimental data.

Conclusion

The main objective of this study is to illustrate the versatility and usefulness of a recently developed nonlinear aerodynamic prediction capability based on the full-potential equation. Results are shown for a variety of complex configurations, including a multibody problem. Comparison of results with available experimental data are in good agreement. The fully vectorized version of this code takes about 4 to 5 min of CPU time for analysis of typical fighter-like configurations on the CYBER 176 computer and about 25-30 s on the CRAY-XMP for a marching plane grid of 70 × 25.

Acknowledgments

This work was partially supported by NASA Langley Research Center under Contract No. NAS1-15820 and by Rockwell International Space Division under IDWA No. M22178, Contract No. NAS9-14000.

References

[1]Shankar, V., Szema, K. Y., and Osher, S., "A Conservation Type-Dependent Full Potential Method for the Treatment of Supersonic Flow with Embedded Subsonic Region," AIAA Paper 83-1887, July 1983.

[2]Szema, K. Y. and Shankar, V., "Nonlinear Computation of Wing-Body-Vertical Tail-Wake Flows at Low Supersonic Speeds," AIAA Paper 84-0427, Jan. 1984.

[3]Siclari, M. J., "The NCOREL Computer Program for 3D Nonlinear Supersonic Potential Flow Computations," NASA CR-3694, Aug. 1983.

[4]Shankar, V., "Implicit Treatment of the Unsteady Full Potential Equation in Conservation Form," AIAA Paper 84-0262, Jan. 1984.

[5]Stack, S. H., Edwards, C. L. W., and Small, W. J., "GEMPAK: An Arbitrary Aircraft Geometry Generator," NASA TP-1022, Dec. 1977.

[6]Tice, S. E., Zolon, J. L., and Repic, R. A., "SVCDS—An Evolutionary CDS for Preliminary Space Vehicle Design, Analysis and Simulation," AIAA Paper 84-2393, Oct. 1984.

From the AIAA Progress in Astronautics and Aeronautics Series . . .

TRANSONIC AERODYNAMICS—v. 81

Edited by David Nixon, Nielsen Engineering & Research, Inc.

Forty years ago in the early 1940s the advent of high-performance military aircraft that could reach transonic speeds in a dive led to a concentration of research effort, experimental and theoretical, in transonic flow. For a variety of reasons, fundamental progress was slow until the availability of large computers in the late 1960s initiated the present resurgence of interest in the topic. Since that time, prediction methods have developed rapidly and, together with the impetus given by the fuel shortage and the high cost of fuel to the evolution of energy-efficient aircraft, have led to major advances in the understanding of the physical nature of transonic flow. In spite of this growth in knowledge, no book has appeared that treats the advances of the past decade, even in the limited field of steady-state flows. A major feature of the present book is the balance in presentation between theory and numerical analyses on the one hand and the case studies of application to practical aerodynamic design problems in the aviation industry on the other.

Published in 1982, 669 pp., 6×9, illus., $45.00 Mem., $75.00 List

TO ORDER WRITE: Publications Dept., AIAA, 1633 Broadway, New York, N.Y. 10019